Materials Today Bio 16 (2022) 100449

Contents lists available at ScienceDirect

Materials Today Bio

journal homepage: www.journals.elsevier.com/materials-today-bio

Tumor-targeted dual-starvation therapy based on redox-responsive micelle nanosystem with co-loaded LND and BPTES

Zhenxiang Fu [a,1], Huiping Du [a,1], Siyu Meng [a], Mengjiao Yao [b], Pan Zhao [a], Xiang Li [b], Xinmin Zheng [b], Zhang Yuan [a,**], Hui Yang [b], Kaiyong Cai [c], Liangliang Dai [a,*]

[a] Xi'an Key Laboratory of Stem Cell and Regenerative Medicine, Institute of Medical Research, Northwestern Polytechnical University, Xi'an, 710072, PR China
[b] School of Life Sciences, Northwestern Polytechnical University, Xi'an, 710072, PR China
[c] Key Laboratory of Bioarcheological Science and Technology, Ministry of Education College of Bioengineering, Chongqing University, Chongqing, 400044, PR China

ARTICLE INFO

Keywords:
Redox-responsive
Degradable micelle
Drug delivery nanosystem
Dual-starvation therapy
Metabolism suppression

ABSTRACT

The starvation therapy mediated by the lonidamine (LND) was limited by the low drug delivery efficiency, off-target effect and compensative glutamine metabolism. Herein, a hyaluronic acid (HA)-modified reduction-responsive micellar nanosystem co-loaded with glycolysis and glutamine metabolism inhibitor (LND and bis-2-(5-phenylacetmido-1,2,4-thiadiazol-2-yl)ethyl sulfide, BPTES) was constructed for tumor-targeted dual-starvation therapy. The *in vitro* and *in vivo* results collectively suggested that the fabricated nanosystem could effectively endocytosed by tumor cells via HA receptor-ligand recognition, and rapidly release starvation-inducers LND and BPTES in response to the GSH-rich intratumoral cytoplasm. Furthermore, the released LND and BPTES were capable of inducing glycolysis and glutamine metabolism suppression, and accompanied by significant mitochondrial damage, cell cycle arrest and tumor cells apoptosis, eventually devoting to the blockade of the energy and substance supply and tumor killing with high efficiency. In summary, HPPPH@L@B nanosystem significantly inhibited the compensatory glycolysis and glutamine metabolism via the dual-starvation therapy strategy, blocked the indispensable energy and substance supply of tumors, consequently leading to the desired tumor starvation and effective tumor killing with reliable biosafety.

1. Introduction

Metabolic reprogramming is a distinct marker of malignant tumors [1]. Meanwhile, both glycolysis and glutamine metabolism played important roles in the cancer proliferation and displayed themselves as natural target sites for antitumor metabolic therapy, since they could provide abundant energy and substance for the rapid growth of tumor [2]. Typically, lonidamine (LND) could significantly kill tumors through selectively inhibiting glycolysis metabolism and blocking energy supply [3,4]. However, its clinical therapeutic effect were limited by low solubility, severe hemolysis and compensatory glutamine metabolism [5]. Therefore, it was necessary to seek a safe and efficient drug delivery strategy functionalized with synergistic glutamine inhibition feature for effective tumor starvation therapy.

Glutamine is well known as a key substance in tumorigenesis and development, and the growth and proliferation of various tumor cells were highly dependent on glutamine metabolism [6]. Glutamine, as an important provider of carbon and nitrogen sources in biosynthesis, was involved in the synthesis of various biological compounds required for tumor reproduction (*e.g.* purine, pyrimidine nucleotides, glucosamine 6-phosphate, and non-essential amino acids) [7,8]. Generally, glutamine was metabolized in the body through the conversion of glutamate to oxoglutaric acid (also known as α-ketoglutaric acid), which entered the TCA cycle as a glutamine-derived carbon. Notably, Glutaminase (GLS1) was a typically rate-limiting enzyme in the above-mentioned glutamine metabolism, which was highly expressed in breast cancer, small cell lung cancer, liver cancers, *etc*. Thus, it was a natural target molecule for tumor glutamine starvation treatment [9,10]. BPTES, the typically allosteric inhibitor of GLS1, could specifically inhibit glutamine metabolism. However, its antitumor therapeutic effect was actually limited by the compensatory glycolysis metabolism [11,12]. Thus, the combined glycolysis and glutamine metabolism suppression strategy could

* Corresponding author.
** Corresponding author.
E-mail addresses: yuanzhang1993@nwpu.edu.cn (Z. Yuan), liangliangdai@nwpu.edu.cn (L. Dai).
[1] These authors contributed equally to this work.

https://doi.org/10.1016/j.mtbio.2022.100449
Received 4 August 2022; Received in revised form 24 September 2022; Accepted 2 October 2022
Available online 3 October 2022

effectively inhibit compensatory metabolism and block the supply of energy and substance, which displayed great potential for cancer therapy. It was important to note that both clinical therapeutic effect of LND and BPTES were hindered by the poor solubility and low bioavailability, which were caused by the off-target effect [13,14]. Therefore, it was necessary to design a tumor-targeted drug delivery nanoplatform with co-loading glycolysis and glutamine metabolism inhibitors for dual-starvation therapy.

Micelles were widely used in drug delivery based on the advantages of good biocompatibility, high drug loading capacity and easy functionalization [15–17]. Given the high expression of characteristic receptors on the surface of most tumors, such as CD44, they were natural targeting motifs for targeted tumor therapy [18–20]. Therefore, the micellar drug delivery system modified with tumor targeting agents (*e.g.* hyaluronic acid, HA) could specifically uptake by tumors via the receptor-mediated endocytosis pathway, which could distinctly avoid off-target effect and improve drug bioavailability. It had been proved to be a safe and efficient tumor-targeted drug delivery strategy [21,22]. Furthermore, redox-responsive drug release mechanism were another common delivery strategy, which could release cargoes *in situ* in response to the reduction stimulus-GSH overexpressed in tumor cells, thereby improving drug bioavailability and tumor therapeutic effect. Therefore, the micellar nanosystem functionalized with tumor targeting motifs and redox-responsive release property was thus a promising alternative strategy for tumor targeting therapy [23–25].

Inspired by the above considerations, herein, HA-functionalized redox-responsive micellar nanosystem was designed to co-load BPTES and LND for tumor-targeted dual-starvation therapy. The polymeric micelle nanosystem was fabricated as follows (Scheme 1): the hydrophobic agent polycaprolactone diol (PCL) was first conjugated with the hydrophilic block of PEI through disulfide bond, forming the initial amphiphilic copolymer PEI–SS–PCL–SS–PEI (abbreviated as PPP); the tumor targeting motif HA was then introduced to the surface of PPP, harvesting the middle product of HA-PEI–SS–PCL–SS–PEI-HA (abbreviated as HPPPH); LND and BPTES were subsequently encapsulated into the polymeric micelle, and yielding the final product of HPPPH@L@B nanosystem. The underlying rationale and advantages of the nanosystem in this work were listed as follows: 1) the nanosystem could significantly accumulate at the tumor site through the passive targeting pathway of the enhanced permeability and retention (EPR) effect and the active targeting pathway of the HA receptor-ligand recognition after systematic administration, which was helpful for prolonging its blood circulation

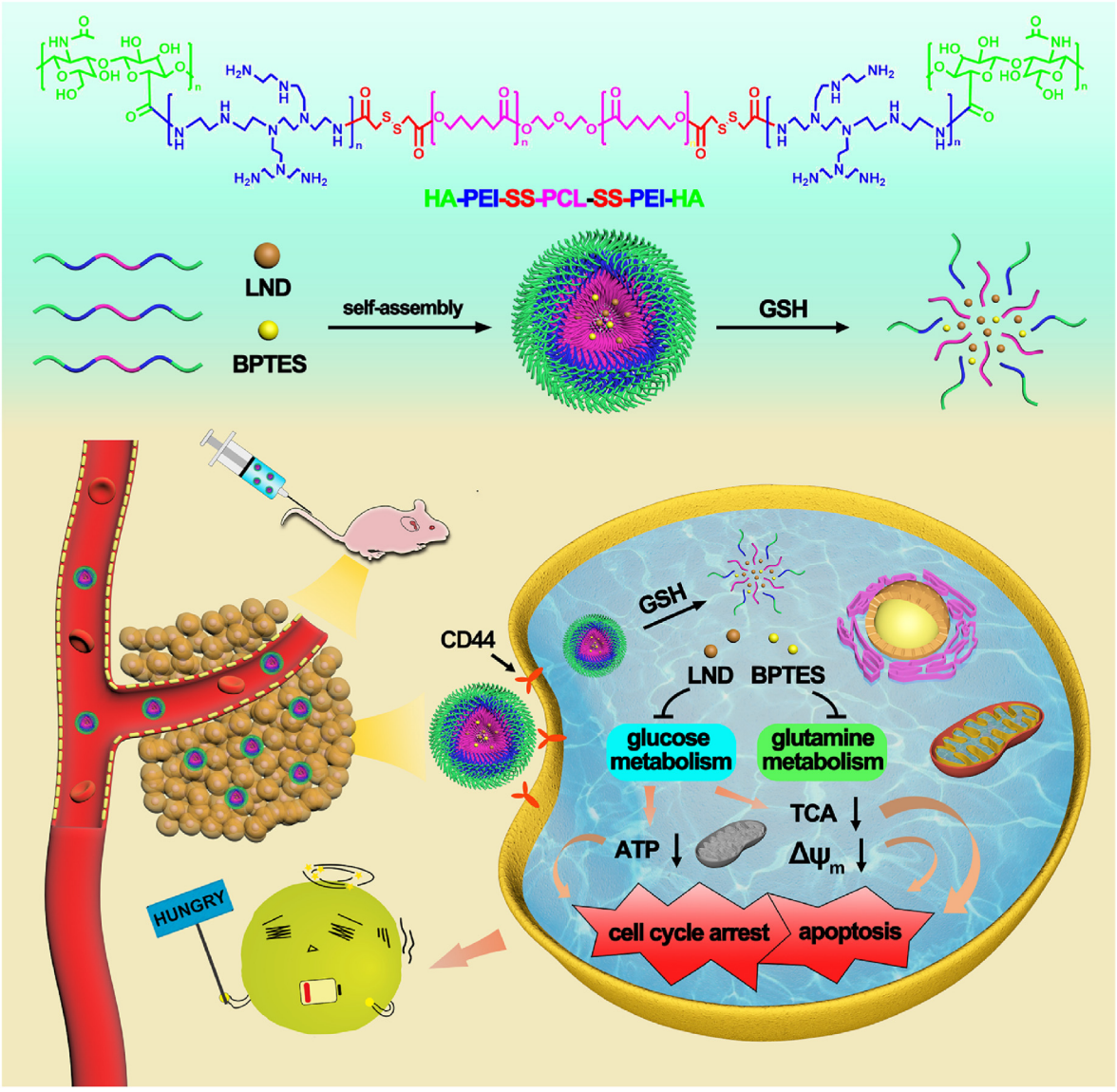

Scheme 1. Construction of the redox-responsive degradable micelle nanosystem HPPPH@L@B and illustration of HPPPH@L@B nanosystem for tumor targeted dual-starvation therapy.

time and reducing off-target effect; 2) the intracellular high concentration of GSH could cleave the disulfide bonds linked the hydrophilic PEI with hydrophobic PCL segments, the hydrophilic-hydrophobic balance maintained the stability of micelle was correspondingly broken, leading to the completed micelle disassembly and drug release; 3) Moreover, the *in situ* released LND and BPTES collectively inhibited the compensatory glycolysis and glutamine metabolism, blocked the indispensable energy and substance supply of tumor cells, leading to the desired tumor starvation and effective tumor killing. Thus, we hypothesized that the redox-responsive degradable micelle nanosystem with HA functionalization could effectively target tumors and suppress tumor growth via the combined effects of glycolysis and glutamine dual-starvation therapy.

2. Materials and methods

2.1. Materials

Polycaprolactone diol (PCL, MW~2000) and N-hydroxy succinimide (NHS) were purchased from Sigma-Aldrich (Beijing, China). Branched polyethyleneimine (PEI, MW 1800) and N,N′-dicyclohexylcarbodiimide (DCC) were purchased from Alfa Aesar (Shanghai, China). Dithiodiglycolic acid, 4-dimethylaminopyridine (DMAP) was purchased from TCI (Shanghai, China). Hyaluronic acid (HA) was purchased from Macklin (Shanghai, China). N, N-dimethylformamide (DMF) and dimethyl sulfoxide (DMSO) were purchased from Aladdin (Shanghai, China). Lonidamine (LND) was purchased from Meilunbio (Dalian, China). BPTES was purchased from Famo biotechnology (Shanghai, China). Primary antibodies including rabbit anti-Bax, rabbit anti-Bcl-2, rabbit anti-PARP, rabbit anti-cytochrome c, rabbit anti-P21, rabbit anti-Cyclin D1, rabbit anti-Cyclin E2 and rabbit anti-Tubulin were obtained from Proteintech (Wuhan, China). Rabbit anti-Ki67 was purchased from Cell Signaling Technology, Inc. Secondary antibody of horseradish peroxidase-conjugated goat IgG was purchased from Beyotime (Jiangsu, China).

2.2. Sample preparation and characterization

2.2.1. Synthesis of COOH-SS-PCL–SS–COOH polymer

PCL (4 g) and DCC (1.65 g) were dissolved into DMF (30 mL) and stirred at 0 °C. Subsequently, the DMF (10 mL) mixture solution dissolved with dithiodiglycolic acid (1.52 g) was added drop by drop to the above solution and stirred for another 30 min at 0 °C. The reaction temperature was then gradually increased to 30 °C, followed by mechanically stirring for 48 h. Next, the mixture solution was filtered, the obtained supernatant was then added drop by drop to cold deionized water, followed by collecting the precipitation. Finally, the product was obtained through washing precipitation with anhydrous ethanol for three times and vacuum drying at 40 °C for 48 h, which was named as COOH-SS-PCL–SS–COOH (77% yield). ^{1}H NMR (400 MHz, DMSO-d_6, ppm, Fig. S1 b, Supporting Information): 1.22 (t, 36H, –$CH_2CH_2CH_2$-), 1.46–1.48 (m, 72H, –$COCH_2CH_2CH_2$- and –$CH_2CH_2CH_2O$-), 2.20 (t, 36H, –$COCH_2CH_2$-), 2.61 (s, 4H, –$COCH_2S$-), 3.63 (t, 4H, –OCH_2CH_2-), 3.75 (s, 4H, –SCH_2COOH), 3.91 (t, 36H, –CH_2CH_2O-), 3.99 (t, 4H, –OCH_2CH_2O-). FTIR (Fig. S2 b): 3438, 2943, 1728, 1635 cm^{-1}. Mass spectrum was characterized in Fig. S3.

2.2.2. Synthesis of PEI–SS–PCL–SS–PEI polymer

COOH-SS-PCL–SS–COOH (174.6 mg), NHS (51.8 mg) and DCC (93 mg) were dissolved into dichloromethane (5 mL). The reaction was stirred at room temperature for 48 h and filtered to remove the precipitate. Subsequently, the obtained supernatant solution was dropped into the DCM solution (10 mL) containing PEI (1.35 g) and stirred for 3 days. The product was concentrated by rotation evaporation, and then re-dissolved with methanol, followed by dialyzing for 48 h. The result product detonated as PEI–SS–PCL–SS–PEI was harvested through freeze-drying (57% yield). ^{1}H NMR (400 MHz, DMSO-d_6: D_2O 70:30 (v/v), ppm, Fig. S1 c): 1.19 (t, 36H, –$CH_2CH_2CH_2$-), 1.43 (m, 72H, –$COCH_2CH_2CH_2$- and –$CH_2CH_2CH_2O$-), 2.10 (t, 36H, –$COCH_2CH_2$-), 2.59–2.82 (m, methylene groups of PEI), 3.83 (t, 36H, –CH_2CH_2O-). FTIR (Fig. S2 c): 3442, 2943, 1568 cm^{-1}.

2.2.3. Synthesis of HA-PEI–SS–PCL–SS–PEI-HA polymer

HA (12 mg, 40–100 KDa), EDC (97.81 mg) and NHS (58.72 mg) were dissolved into NaCl solution (1 M) and stirred for 1.5 h. Subsequently, 30 mL of PBS (pH 6.5) dissolved with PEI–SS–PCL–SS–PEI (59 mg) was then slowly added to above solution. After stirring for 24 h, the mixture solution was dialyzed (MWCO 10 kDa) against double-distilled water for 48 h. The final product HA-PEI–SS–PCL–SS–PEI-HA was obtained via freeze-drying (92% yield). ^{1}H NMR (400 MHz, DMSO-d_6: D_2O 70:30 (v/v), ppm, Fig. S1 d): 1.31 (t, 36H, –$CH_2CH_2CH_2$-), 1.55 (m, 72H, –$COCH_2CH_2CH_2$- and –$CH_2CH_2CH_2O$-), 3.75 (s, 4H, –SCH_2COOH), 2.23 (t, 36H, –$COCH_2CH_2$-), 2.63 (m, methylene groups of PEI), 3.83 (t, 36H, –$COCH_3$-). FTIR (Fig. S2 d): 3440, 2945, 1725, 1046 cm^{-1}.

2.2.4. Preparation of blank micelle and drug loaded micelle

Both blank and drug-loaded micelle were prepared by water-oil emulsion-solvent evaporation method. Typically, HA-PEI–SS–PCL–SS–PEI-HA (16 mg), LND (6 mg) and BPTES (2 mg) dissolved into 2 mL of DMSO. The mixture solution was stirred at room temperature for 4 h, the obtained solution was then dropped into 10 mL of distilled water and stirred for another 24 h. Finally, the reaction solution was dialyzed (MWCO 500 Da) against distilled water for 4 days. The final product named as HPPPH@L@B was collected through freeze-drying. For one thing, the mixture containing just HA-PEI–SS–PCL–SS–PEI-HA and LND were prepared via above same method, which was harvested and named as HPPPH@L. For another thing, the mixture containing only HA-PEI–SS–PCL–SS–PEI-HA or PEI–SS–PCL–SS–PEI were prepared via above same method as well, and the obtained blank micelles were donated as HPPPH and PPP, respectively. Besides, UV/Vis spectrometer and the standard curves of LND at 300 nm and BPTES at 270 nm were used to monitor the drug loading content (DLC) and drug loading efficiency (DLE), which were calculated by the following equations:

$$\text{DLC}\ (\%) = \text{Amount of loaded drug} \,/\, \text{Weight of drug loaded copolymer} \times 100\%$$

$$\text{DLE}\ (\%) = \text{Amount of loaded drug} \,/\, \text{Weight of drug in feed} \times 100\%$$

2.2.5. Materials characterization

The structure and molecular weight of the various polymers were measured by ^{1}H NMR (Bruker Avance 400 MHz, Germany), fourier transforms infrared spectroscopy (FTIR, model 6300, BioRad Co. Ltd., USA), mass spectrometry (Waters Acquity SQ Detector UPLC-MS) and gel-permeation chromatograph (GPC, Alliance e2695, Waters). The eluent of GPC used was DMF or double-distilled water, and the flow rate was 1.0 mL min^{-1} at 40 °C. The morphology, size distribution, surface charge of micelles were characterized by TEM (Talos F200X TEM, FEI), zeta potential measurement (Brookhaven 90 Plus PALS, Brookhaven) equipped with DLS, respectively. HPLC (Waters Alliance HPLC e2695, Waters) was performed on a C18 column (XAqua, 4.6 × 250 mm, 5 μm, Acchrom) using a linear gradient of acetonitrile and DI water (51:49, vol/vol) containing 0.1% trifluoracetic acid as a mobile phase, and the flow rate was 1.0 mL min^{-1} at 29 °C.

2.2.6. Stability and critical micelle concentration (CMC) of HPPPH@L@B assays

As for the stability assay, PPP@L@B or HPPPH@L@B micelles was firstly incubated in PBS solution (pH 7.4) containing 10% FBS at 37 °C. Subsequently, the average size of samples were monitored by DLS at certain time intervals (0, 6, 12, 24, 48, 72, 96, 120 and 144 h). The change in size was used to characterize the degree of adsorption of micelles to FBS and its stability. As for the CMC detection, pyrene dissolved

in acetone (6×10^{-6} M) was firstly evaporated under nitrogen protection. Next, HPPPH copolymer with different concentrations (10^{-3} to 10^{-8} g/mL) were added to above mixture. Meanwhile, the dose of pyrene was adjusted to 6×10^{-7} M. Subsequently, above samples were equilibrated in a shaker under dark environment for 24 h. The excitation spectra of above samples were analyzed at wavelengths ranging from 300 to 380 nm and an emission wavelength of 390 nm, detected by a fluorescence spectrophotometer. Finally, the intensity ratios (I338/I333) versus the logarithm of sample concentrations were plotted. The detailed experiment procedures were referred to the previous literature [26].

2.2.7. Drug release behavior

Typically, the HPPPH@L@B micelles (3 mg) were firstly dispersed into 1 mL of PBS buffer (pH 7.4) containing different concentrations of GSH (0 mM, 2 mM, 10 mM) and transferred into dialysis bags (MWCO 3.5 kDa). The above mixture was then immersed into 9 mL of the same solution containing various dose of GSH with shaking at 37 °C under dark environment. At specific time intervals, 0.6 mL of external liquid was taken out for detection and the same volume of fresh PBS containing various dose of GSH was added correspondingly. Drug concentration was measured by UV/Vis spectrophotometer (Hitachi U-3900).

2.3. In vitro study

2.3.1. Cell culture and cytotoxicity assays

MDA-MB-231 cell lines were purchased from the Cell Bank of the Chinese Academy of Sciences (Shanghai, China). MDA-MB-231 cells were cultured with Dulbecco's modified Eagle's medium (DMEM) containing 10% FBS, and 1% penicillin-streptomycin with 5% CO_2 at 37 °C.

Cell cytotoxicity assay was employed using CCK-8 kit (Beyotime). Briefly, the cells were firstly implanted in 24-well plates at a density of 2×10^4/well. When the cell density reached to 60–70%, HPPPH, LND (15 μg/mL), HPPPH@L (65.2 μg/mL) and HPPPH@L@B (65.2 μg/mL, as same dosage of LND) were added and co-incubated with MDA-MB-231 cell for 24 h or 48 h. Subsequently, the cells were washed with PBS, followed by co-culturing with 200 μL fresh medium and 20 μL CCK-8 solution at 37 °C for 1.5 h. Afterwards, the supernatant was transferred to a 96-well plate and measured with a microplate reader (Tecan Spark, Tecan) at 450 nm.

2.3.2. In vitro cellular uptake

Confocal microscopy and flow cytometry were used to detect the uptake level of micelles by MDA-MB-231 cells. Typically, the cells were inoculated into confocal microscopy dishes or 6-well plates, and then treated with model drug of Nile red (10 μg/mL), PPP@Nr without HA conjugation (85.6 μg/mL) and HPPPH@Nr (85.6 μg/mL) with or without HA (5 mg/mL HA pretreatment for 2 h) for 12 h and 24 h, respectively. For the confocal laser scanning microscopy (CLSM) analysis, cells seeded on confocal microscopy dishes were washed with PBS and fixed with 4% paraformaldehyde, permeabilized with 0.2% Triton, the cytoskeleton and nucleus were respective stained with Alexa 488-phalloidin and DAPI. Finally, the cells were imaged with CLSM (FV3000, Olympus, Japan). For the flow cytometry (FCM) analysis, cells seeded on 6-well plates were digested, collected by centrifugation, re-suspended in PBS solution and analyzed by FCM (BD, Biosciences).

2.3.3. Cell apoptosis assay

Annexin V-FITC/PI apoptosis detection kit was used to detect cell apoptosis levels. Briefly, the cells cultured in six-well plates were treated with HPPPH, LND (15 μg/mL), HPPPH@L (65.2 μg/mL) and HPPPH@L@B (65.2 μg/mL, as same dosage of LND) for 24 h, respectively. The cells were subsequently collected by centrifugation, stained using Annexin V-FITC/PI kit (Beyotime, China) and detected by FCM.

2.3.4. Western bolt assay

Apoptotic pathway-associated proteins in MDA-MB-231 cells treated with various formulations were examined by Western blotting. Briefly, MDA-MB-231 cells were seeded on 6-well plates and then treated with HPPPH, LND (15 μg/mL), HPPPH@L (65.2 μg/mL) and HPPPH@L@B (65.2 μg/mL, as same dosage of LND) for 24 h. Subsequently, cell samples were washed with PBS and solubilized with lysis buffer. Next, the total proteins were harvested by centrifugation (12,000 rpm 10 min, 4C), BCA protein assay kit (Beyotime) was used to determine the protein concentration. Finally, the protein bands were visualized by enhanced chemiluminescence (ECL) detection reagents and captured using imaging system (Vilber fusion FX6. EDGE). The quantitative data analysis was performed with ImageJ software.

2.3.5. Mitochondrial damage detection

The typically JC-1 fluorescent dye was used to detect the changes of mitochondrial membrane potential [27]. The MDA-MB-231 cells cultured in confocal microscopy dishes were treated with HPPPH, LND (15 μg/mL), HPPPH@L (65.2 μg/mL) and HPPPH@L@B (65.2 μg/mL, as same dosage of LND) for 12 h, respectively. Next, the cells were washed with PBS and stained with mitochondrial membrane potential assay Kit (Beyotime) according to the manufacturer's protocols. Finally, the cells were detected by CLSM.

2.3.6. Cell cycle arrest assay and related protein expression analysis

Briefly, the MDA-MB-231 cells were cultured in 6-well plates and treated with HPPPH, LND (15 μg/mL), HPPPH@L (65.2 μg/mL) and HPPPH@L@B (65.2 μg/mL, as same dosage of LND) for 24 h. Subsequently, the cells were washed, collected and stained with PI according to the manufacturer's protocols. Finally, the DNA content in the G0/G1, S, and G2 phases of cells and related quantitative analysis were detected by FCM. In addition, the expression levels of cyclin-related proteins P21, Cyclin D1 and Cyclin E2 were further measured by western blotting. The detailed experiment procedures were referred to the above western blotting assay.

2.3.7. Intracellular ATP content study

The intracellular content of ATP was measured using the ATP detection kit. Typically, the MDA-MB-231 cells were cultured in 6-well plates and treated with HPPPH, LND (15 μg/mL), HPPPH@L (65.2 μg/mL) and HPPPH@L@B (65.2 μg/mL, as same dosage of LND). After incubation for 24 h, the cells were lysed and collected by centrifugation, and the concentration was determined by using BCA protein assay Kit (Beyotime). Finally, the intracellular ATP content of above samples were detected by multi-function microplate analyzer according to the manufacturer's protocols.

2.3.8. Metabolomics study

The MDA-MB-231 cells seeded in the 75 cm^3 flasks were treated with HPPPH, LND (15 μg/mL), HPPPH@L (65.2 μg/mL) and HPPPH@L@B (65.2 μg/mL, as same dosage of LND). After 24 h incubation, the cells were washed with PBS and collected by cell scraper, followed by freezing with liquid nitrogen. Finally, the samples were sent to the Lc-Bio Technologies company for metabolomics analysis.

2.4. In vivo study

2.4.1. Establishment of xenograft tumor model and antitumor therapy in vivo

BALB/c male nude mice (5–6 weeks) were purchased from Beijing Institute for Drug Control. All animal experiments were strictly performed according to guidelines of the Institutional Animal Care and Use Committee of China. For the establishment of the mouse xenotransplantation model, 100 μL of saline containing 5×10^6 MDA-MB-231

cells was subcutaneously injected into the right groin of mouse. When the tumor size reached to about 50 mm^3, the mice were randomly divided into five groups and intravenously injected with saline, HPPPH, LND, HPPPH@L and HPPPH@L@B at the dose of 10 mg/kg LND equivalent (n = 6). The above administrations were given twice a week and lasted for 18 days. Meanwhile, the body weight and tumor volume were recorded every two days. Tumor volume was calculated as follows: tumor volume = $ab^2/2$ (a: the maximum dimension of the tumor, b: the minimum dimension of the tumor). Additionally, the survival rate of mice was monitored for another 25 days after the last administration.

2.4.2. H&E, TUNEL and immunofluorescence staining assays

The mice were euthanized after the last administration. The major organs and tumor of mice were collected, fixed, embedded, sliced and stained with hematoxylin and eosin for H&E histological analysis. Meanwhile, the tumor sections were de-paraffinized and stained with the In Situ Cell Death Detection Kit (Beyotime) for TUNEL apoptosis analysis. In additional, the tumor sections de-paraffinized were also stained with Ki67 primary antibody and FITC-labelled fluorescent secondary antibody for immunofluorescence staining analysis.

2.4.3. Blood safety study

HPPPH@L@B along with control (saline) were intravenously injected into the mice. The blood was collected after 24 h of administration. The blood biochemical levels and hematological indices were measured according to the manufacturer's protocols.

2.4.4. Pharmacokinetics and biodistribution

MDA-MB-231 cell tumor-bearing nude mice were intravenously injected with LND and HPPPH@L@B at a dose of 10 mg/kg LND. Subsequently, blood was collected from orbital venous plexus after administration of 10 min, 30 min, 1 h, 4 h, 8 h, 12 h and 24 h, respectively. The blood sample was then immediately centrifuged (2000 g, 10 min) to obtain the supernatant for pharmacokinetics analysis using HPLC. In terms of biodistribution, the mice were euthanized at 24 h after intravenous injection of LND and HPPPH@L@B. The liver, lung, kidney, spleen, heart and tumor of mice were collected and weighed. The tissues were then homogenized in buffer containing 10 mM Tris, 1 mM EDTA and 10% (V/V) glycerol (pH 7.4) (W/V ratio 1:10). The sample was centrifuged at 16,000 g for 15 min. Next, the supernatant was separated and extracted with ethyl acetate at a ratio of 1:1.3 (vol/vol). The solution was then dried under nitrogen and the dry powder was re-dissolved in methanol for analysis by HPLC. The distribution of LND in tissues was calculated as μg (amount of LND) per g (wet weight of tissues).

3. Results and discussion

3.1. The synthesis and characterization of HPPPH@L@B nanosystem

The final copolymer was synthesized through multiple chemical-conjugated reactions. Briefly, polycaprolactone (PCL, MW 2000) as a hydrophobic segment was firstly grafted with hydrophilic reagent of PEI (MW 1800) via GSH-cleaved linker of dithiodiglycolic acid, forming the initial amphiphilic polymer PEI–SS–PCL–SS–PEI (abbreviated as PPP). Next, the tumor targeting molecule hyaluronic acid (HA) was covalently conjugated to the surface of PPP block copolymer, obtaining the final product of HA-PEI–SS–PCL–SS–PEI-HA (abbreviated as HPPPH). As shown in Fig. S1 (Supporting Information), the typical resonances at 2.63 ppm and 3.75 ppm & 3.83 ppm were attributed to the protons in PEI and HA molecules, respectively. It was clearly suggested the successful conjugation of PEI and HA into COOH-SS-PCL–SS–COOH agents. Furthermore, ^1H NMR and FTIR spectra further revealed the successful stepwise functionalization of the various copolymers (Figs. S1 and S2). Moreover, the average molecular weights of various intermediate products were accordingly increase with the stepwise conjugation processes (increased from 3100 of PCL to 114600 of HA-PEI–SS–PCL–SS–PEI-HA), detected by mass spectrum (MS, Fig. S3) and gel-permeation chromatography (GPC, Fig. 1a). The results also showed the excellent consistence with their theoretical values (Table S1), indicating again the successful synthesis of the final copolymer of HA-PEI–SS–PCL–SS–PEI-HA.

The blank and drug loaded micelles were then fabricated by an oil-in-water emulsion method using the above synthesized copolymer as precursor, according to a previous study [28]. The critical micelle concentration (CMC) was measured with a fluorescent method using pyrene as probe. It was observed that the fluorescence intensity gradually increased with enlarged concentration of HPPPH, and accompanied by a red shift from 333 to 338 nm (Fig. S4), suggesting the formation of micelles. Meanwhile, the blank micelles HPPPH displayed a relatively low CMC with 4.6×10^{-3} g L^{-1} through calculation, which would contribute to the nanosystem stability against the dilution effect of blood circulation *in vivo* [28], implying the good stability. In other words, HPPPH nanosystem with lower CMC could still maintain their stability after being injected into the blood and would not be disintegrated due to surface tension, which was beneficial to improve the safety and efficacy of cargoes. After co-loading with LND and BPTES, HPPPH@LND@BPTES micelles (donate as HPPPH@L@B) exhibited the distinctive absorption peaks same to free BPTES and LND at 270 nm and 300 nm (Fig. S5), suggesting the successful encapsulation of BPTES and LND in HPPPH@L@B micelles. Furthermore, the drug loading content (DLC) and drug loading efficiency (DLE) of LND and BPTES in HPPPH@L@B were quantitatively calculated as 23%, 42.3% and 10%, 53.9%, according to the correspondingly standard curves (Fig. S6).

Subsequently, the morphology, particle size and surface charge traits of the previously constructed HPPPH@L@B micelles were further characterized by transmission electron microscopy (TEM), dynamic light scattering (DLS) and zeta potential, respectively. As demonstrated on Fig. 1b, both PPP@L@B and HPPPH@L@B showed a well-defined spherical morphology, suggesting the successful preparation of drug loaded micelles. Furthermore, the diameter of HPPPH@L@B gradually increased from 60 nm to around 110 nm after the introduction of HA, which was consistent with DLS data (Fig. 1c), revealing the successful conjugation of HA agents. Meanwhile, the surface charge of HPPPH@L@B micelles was also reversed from +33 mV to −9 mV (Fig. 1d), owing to the successful introduction of HA with strong negative charge property. Besides, the biostability of micelles was further investigated by dissolving micelles in 10% fetal bovine serum (FBS) and measuring its size change by DLS. The size of PPP@L@B nanosystem displayed the dynamical increase upon 6 days (Fig. 1e), it was caused by the electrostatic adsorption between positively charged PPP@L@B micelle and negatively charged FBS [28]. In contrast, the size of HPPPH@L@B nanosystem shown a negligible increase upon same condition, resulting from the actual charge repulsion between the HA-modified HPPPH@L@B with negative charge and FBS. All above results suggested that HPPPH@L@B nanosystem with good biostability had been successful constructed.

To reveal redox-responsive micelle disassembly and drug release features, 10 mM GSH (stimulation tumor microenvironment) was used to co-cultured with HPPPH@L@B micelle nanosystem, the change of morphology, particle size and drug release behavior of nanosystem were monitored by TEM, DLS and absorption spectrum, respectively. As shown in Fig. 1b, both the morphology of PPP@L@B and HPPPH@L@B micelles transferred from the intact spherical to the collapse structure after treatment with GSH for 4 h, which was consistence with DLS, implying the distinct micelle disassembly. Meanwhile, the intensity of absorption peaks of BPTES and LND in HPPPH@L@B micelles shown an obviously increase after culturing with GSH, owing to the certain BPTES and LND release (Fig. S5). In order to further quantitatively monitor the drug release behavior of nanosystem, the real-time release profile of LND in HPPPH@L@B nanosystem upon different doses of GSH were measured.

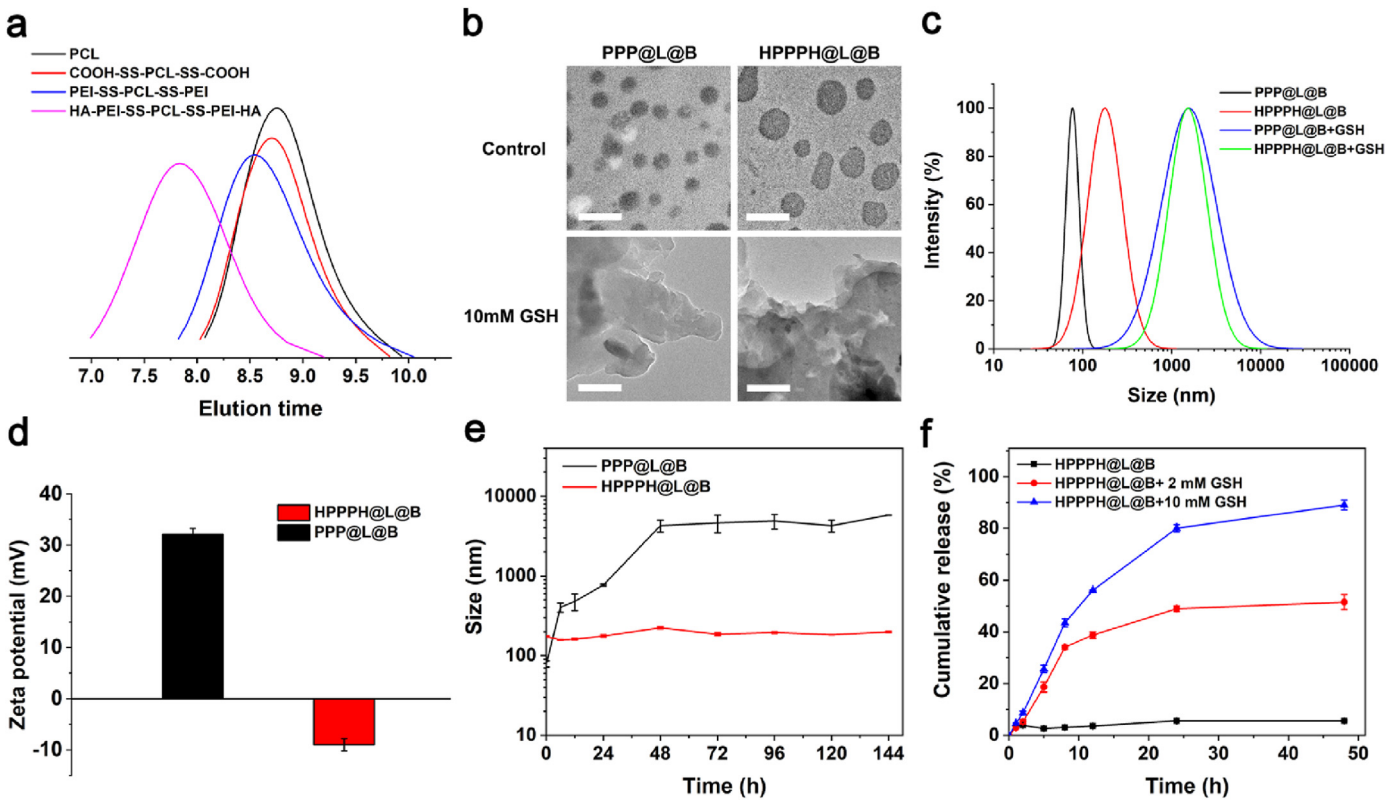

Fig. 1. Micellar characterization. (a) GPC profile of PCL, COOH-SS-PCL–SS–COOH, PPP and HPPPH polymers. (b) TEM images and (c) DLS data of PPP@L@B and HPPPH@L@B micelles with or without 10 mM GSH incubation. Scale bar: 200 nm. (d) Zeta potential values of PPP@L@B and HPPPH@L@B in PBS (pH 7.4). (e) Size change of PPP@L@B and HPPPH@L@B micelles incubated in PBS solution (pH 7.4) containing 10% FBS for different time intervals. (f) Cumulative release behavior of LND from HPPPH@L@B nanosystem after treatment with various concentrations of GSH upon 48 h. Scale bars: 200 nm for (b). Error bars present as mean ± SD (n = 6).

As displayed in Fig. 1f, HPPPH@L@B exhibited a negligible drug release (around 6%) upon PBS (pH 7.4, stimulation physiological condition) for 48 h, suggesting the good encapsulation trait. It thus didn't leak the drug in the blood with reduced side effects. Excitingly, about 52% and 89% LND were released from HPPPH@L@B nanosystem after respective treatment with 2 mM or 10 mM GSH for 48 h, revealing the complete drug release upon 10 mM GSH condition, which is benefited for effective tumor killing. Above GSH-responsive drug release behavior was also confirmed by BPTES release curve in HPPPH@L@B nanosystem (Fig. S7). Above phenomena could be explained that GSH caused the cleave of the disulfide bond conjugated hydrophobic block of PCL and hydrophilic agent of PEI, and broken the hydrophilic-hydrophobic balance maintained the stability of micelle nanosystem, leading to the rapid micelle disintegration and drug release. These results collectively suggested that HPPPH@L@B nanosystem indeed displayed good biostability under physiological condition and effectively redox-responsive micelles disassembly and drug release property upon tumor microenvironment, which were suitable for tumor therapy *in vivo*.

3.2. Cytotoxicity and the targeted cellular uptake of HPPPH@L@B nanosystem

The cell viability of the MDA-MB-231 tumor cells was subsequently evaluated using CCK-8 kit after co-incubation with HPPPH@L@B nanosystem for 24 h and 48 h, respectively. As showed in Fig. 2a, regardless of incubation time, the viability of MDA-MB-231 cells treated with HPPPH micelle showed no significant difference to control group, suggesting the good biocompatibility of the blank HPPPH micelle. Meanwhile, the HPPPH@L group induced more severe toxicity on MDA-MB-231 cells than LND group either 24 h or 48 h incubation. It could be explained by the fact that drug-loaded micelles HPPPH@L could actually improve the solubility of the hydrophobic drug LND and enhance its bioavailability, the delivered LND can effectively damage tumor cells via the natural inhibition of glycolysis [29]. Notably, the HPPPH@L@B caused the lowest cell viability on MDA-MB-231 cells among all the treatment groups after incubation for 24 h ($p < 0.01$), and the cytotoxicity tendency further increased when the incubation time extended to 48 h. It was attributed to the additional tumor damage caused by the BPTES via suppressing the essential glutamine metabolism [30]. The results suggested that HPPPH@L@B nanosystem possessed a superior tumor killing effect *in vitro*.

In order to prove the targeted uptake performance of the MDA-MB-231 tumor cells against HPPPH@L@B nanosystem, the hydrophobic fluorescent dye Nile Red was chosen as model drug and loaded into the HPPPH micelles (donated as HPPPH@Nr), MDA-MB-231 cells were subsequently incubated with HPPPH@Nr nanosystem for different time intervals, CLSM and FCM were used to monitor the endocytosis efficiency of nanosystem. As showed in Fig. 2b, the Nile Red loaded micelle formulations (PPP@Nr and HPPPH@Nr micelle) labelled with red fluorescence exhibited higher cell uptake efficiency than control and free Nile Red negative groups, regardless of the incubation time. It was attributed to the superior drug delivery efficiency of the micelle nanocarriers [31]. Meanwhile, the endocytosis degree of the HPPPH@Nr was significantly higher than PPP@Nr group after incubation for 12 h or 24 h (Fig. S8). It might cause by the HA-mediated tumor-targeted endocytosis pathway [32,33]. In order to further verify the tumor-targeted endocytosis behavior caused by HA, MDA-MB-231 cells overexpressed with CD44 molecule (HA receptor) were pre-incubated with excessive HA molecules for blocking HA receptors before co-incubation with HPPPH@Nr micelles [34]. The result displayed that the endocytosed amount of

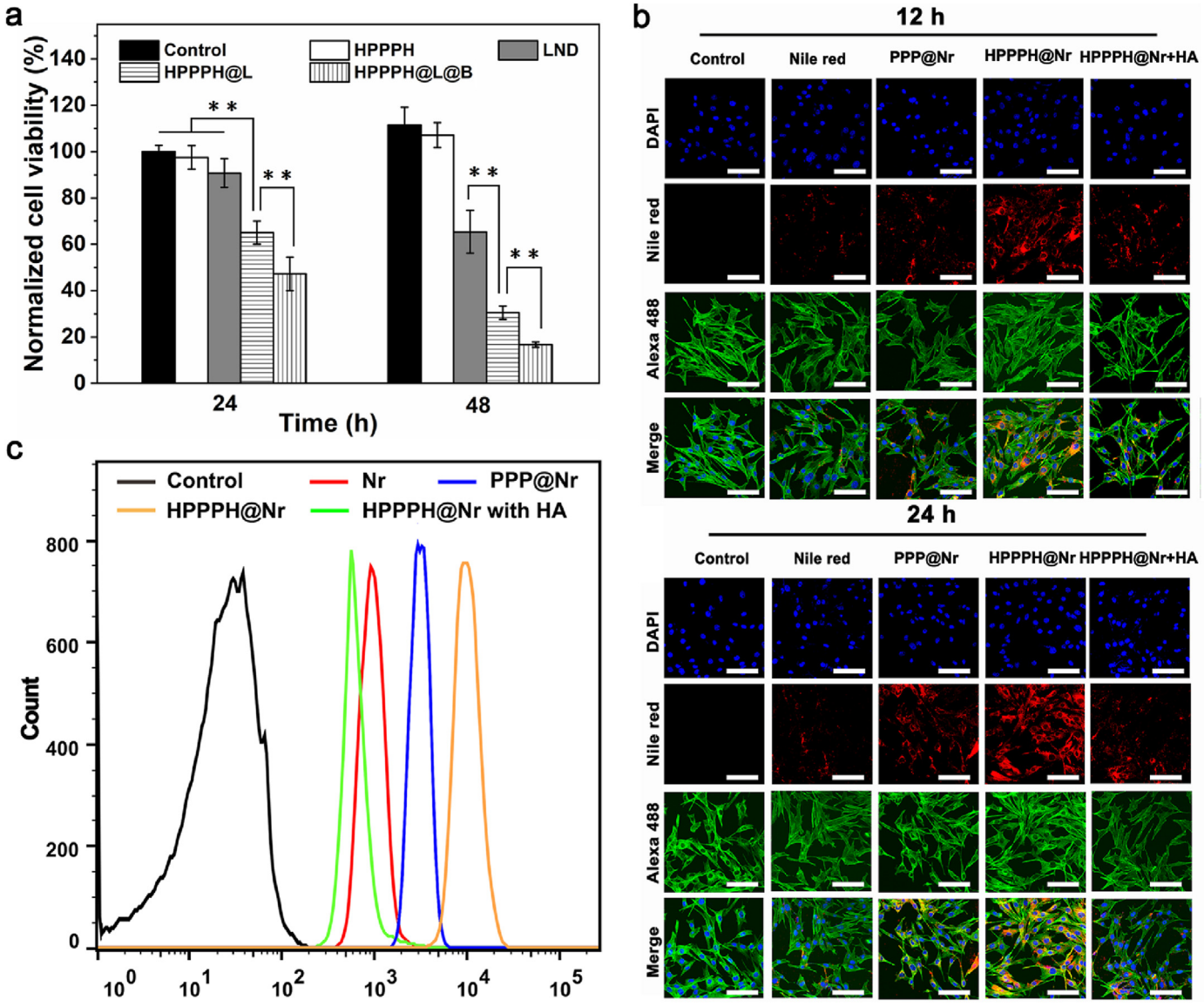

Fig. 2. Cytotoxicity and cellar uptake. (a) Cytotoxicity assay of MDA-MB-231 cells cultivated with PBS (control), HPPPH (65.2 μg/mL), LND (15 μg/mL), HPPPH@L (65.2 μg/mL) and HPPPH@L@B (65.2 μg/mL, as same dosage of LND) for 24 h and 48 h, respectively. (b) Cellular uptake and intracellular distribution of nanosystem in the MDA-MB-231 cells were detected by CLSM after incubation with PBS, Nile Red (model drug), PPP@Nr without HA conjugation, HPPPH@Nr or HPPPH@Nr + HA (pretreatment with HA for 2 h) for 12 h and 24 h, respectively. Nuclei and cytoskeleton were respective stained with DAPI (blue) and Alexa 488-phalloidin (green). (c) Corresponding quantitative FCM analysis of cellular uptake in MDA-MB-231 cells, after above treatments 24 h, respectively. Scale bar: 50 μm for (b). Error bars present as mean ± SD (n = 6), **p < 0.01. (For interpretation of the references to colour in this figure legend, the reader is referred to the Web version of this article.)

HPPPH@Nr micelles in MDA-MB-231 cells was significantly decrease after 12 h incubation, compared to the same group in the absence of HA, as revealed by the relatively lower red fluorescence. The above cellar uptake behavior became more obvious as the incubation time extended to 24 h, which was in consistence with the quantitative FCM analysis (Fig. 2c). The result confirmed that the excellence uptake performance of nanosystem was actually performed by HA receptor-mediated endocytosis. The reason could be explained that HA functionalized nanosystem could specially target tumor cells overexpressed CD44, the nanosystem thus endocytosed by tumor cells through a HA receptor-ligand recognition pathway, which was consistent with a previous result [35]. The result suggested that HPPPH nanosystem could uptake by the tumor cells with high efficiency via HA-mediated endocytosis, which was helpful for tumor killing *in vitro* and *in vivo*.

3.3. Tumor cells apoptosis, mitochondrial damage and cell cycle arrest induced by the HPPPH@L@B nanosystem in vitro

Since the cell viability is closely associated with the initial occurrence of the apoptosis or the cell proliferation [36], and HPPPH@L@B nanosystem could certainly induce a decrease in cell viability, the related apoptosis/death and cell cycle status were subsequently measured in detail. For one thing, the apoptosis/death degree of the MDA-MB-231 cells were investigated using the Annexin V-FITC/PI staining kit and detected by FCM analysis. As shown in Fig. 3a and b, the blank nanocarrier HPPPH caused a negligible apoptosis and death ratio as similar to control group (PBS, about 5%), implying the good biocompatibility. Both LND and HPPPH@L groups induced the moderate cell apoptosis, as revealed by around 10% and 25% apoptosis and death rate, respectively.

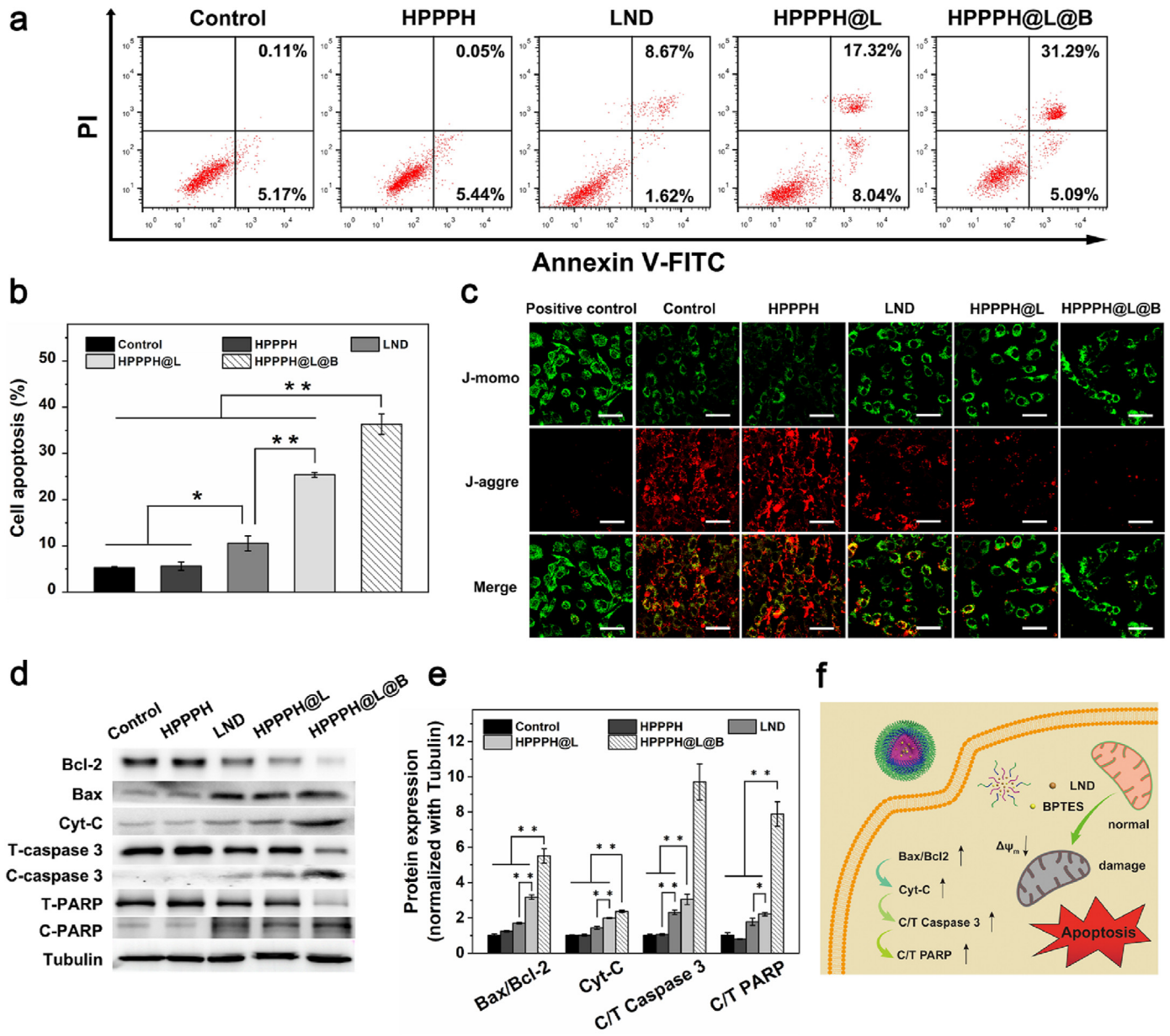

Fig. 3. Apoptosis and mitochondrial damage evaluation. (a) Cell apoptosis level and (b) quantitative analysis of MDA-MB-231 induced by PBS (control), HPPPH, LND, HPPPH@L and HPPPH@L@B after 24 h of incubation, detected by FCM. (c) Mitochondrial membrane depolarization of MDA-MB-231 cells was detected by CLSM after above treatments via JC-1 probe staining. (d) The expression level of the apoptosis related proteins in MDA-MB-231 cells was detected by Western blotting after above treatments for 24 h and (e) the corresponding quantitative analysis via Image J software. (f) Schematic representation of the mitochondrial damage and cell apoptosis pathway in tumor cells induced by HPPPH@L@B nanosystem. Scale bar: 50 μm for (c). Error bars present as mean ± SD (n = 6); *p < 0.05, **p < 0.01.

It was caused by the inherent cytotoxicity of LND and the excellent drug delivery efficiency of HPPPH nanocarrier [37]. Furthermore, HPPPH@L@B group induced the highest apoptosis and death level ($p < 0.01$), implying the superior antitumor effect *in vitro*. It might attribute to the combined effect of glucose and glutamine metabolism inhibition induced by LND and BPTES in the HPPPH@L@B nanosystem, which was investigated in the following section of the cellular metabolic suppression.

To reveal the molecular mechanism of apoptosis induced by HPPPH@L@B nanosystem, the mitochondrial damage evaluation was firstly investigated, resulting from the damage or depolarization of the mitochondria is a typical marker of apoptosis [38,39]. The membrane-permeable JC-1 dye was used to monitor the damage of the mitochondria and the change of mitochondrial membrane potential. It is attributed to the fact that JC-1 could exhibit different existing state in normal/damage mitochondria and emit different fluorescence (red fluorescence, preferential aggregation in the normal mitochondria *vs.* green fluorescence, monomer formation in the cytoplasm) [40]. After treatment for 12 h, LND, HPPPH@L and HPPPH@L@B induced various degree of the mitochondrial damage compared to control and HPPPH negative control groups, as revealed by the decreased red fluorescence and increased green fluorescence, in sequence with LND < HPPPH@L < HPPPH@L@B (Fig. 3c and Fig. S9). It due to the fact that the superior delivery efficiency of the micelle carriers (HPPPH@L and HPPPH@L@B) amplified mitochondrial damage effect mediated by LND [41,42], and the introduction of BPTES might accelerate the mitochondrial damage via suppressing glutamine metabolism additionally [43], leading to the most severe mitochondrial damage and cells apoptosis.

Subsequently, the molecular mechanism of apoptosis and mitochondrial damage induced by HPPPH@L@B nanosystem was further studied

by western blotting assay. Typically, the expression of the proteins that were closely associated with apoptosis pathway and mitochondrial apoptotic pathway, such as Bax, Bcl-2, caspase-3, poly (ADP-ribose) polymerase (PARP) and cytochrome *c*, were measured by western blotting [44,45]. After co-incubation with above formulations for 24 h, both LND and HPPPH@L groups induced the obvious downregulation of Bcl-2, total caspase 3 (donated as T-caspase 3) and total PARP (donated as T-PARP), and the upregulation of Bax, cleaved caspase 3 (donated as C-caspase 3) and cleaved PARP (donated as C-PARP) in MDA-MB-231 cells compared to control and HPPPH negative control groups (Fig. 3d), implying the activation of the apoptosis pathway. Furthermore, the correspondingly quantitative analysis of Bax/Bcl-2, Cyt-c, C/T caspase 3 and C/T PART ratio induced by HPPPH@L group was significantly higher than that of LND group, attributed to the improved drug delivery efficiency and bioavailability. More importantly, the above expression tendency of the associated apoptosis proteins further increased in HPPPH@L@B treatment, which was in consistence with the correspondingly quantitative analysis ($p < 0.01$, Fig. 3e). The result confirmed again that HPPPH@L@B nanosystem actually generated the effective activation of the apoptosis pathway and superior tumor killing effect. On the basis of the results, the apoptosis/death pathway and mitochondrial apoptotic pathway induced the nanosystem might be illustrated as follows (Fig. 3f): the HPPPH@L@B nanosystem endocytosed by the MDA-MB-231 cells could rapidly release LND and BPTES in response to the GSH-rich intracellular environment. The co-work of LND and BPTES could effectively depolarize the mitochondrial membrane potential and damage mitochondria, leading to the initiation of apoptosis and regulation of Bcl-2 protein family. Cytochrome *c* was then released from mitochondria upon stimulation of the aforementioned apoptotic signal, the Caspase 3 acts as an executor of apoptosis was subsequently activated and further promoted cell apoptosis through the cascade activation of PARP, consequently leading to the superior tumor killing *in vitro*.

For another thing, the cell cycle arrest of the MDA-MB-231 cells was investigated by FCM, since starvation therapy mediated by HPPPH@L@B nanosystem could actually block the supply of cellular energy and substance and induce the change of cell cycle [46–48]. Consistent with the cell viability result (Fig. 2a), HPPPH@L treatment induced the significant decrease in the number of cells stayed in the S and G2 phase compared with LND group (Fig. 4a and b and Fig. S10), due to the improved bioavailability of LND in the micelle nanocarrier. It was worth noting that this downward trend was significantly higher in HPPPH@L@B than that in HPPPH@L ($p < 0.01$), as revealed by the lowest amount of the cells remained in the S and G2 phase, indicating the effective G1 phase arrest and cell proliferation inhibition. In order to verify the mechanism of the cell cycle arrest induced by HPPPH@L@B nanosystem, the expression of the related G1 phase proteins were then measured by western blotting, including p21, cyclin D1 and cyclin E2. As shown in Fig. 4c and d, LND, HPPPH@L and HPPPH@L@B induced various extents downregulation of P21 proteins in the MDA-MB-231 cells, and upregulation of Cyclin D1 and Cyclin E2 proteins, in sequence with LND < HPPPH@L < HPPPH@L@B, implying the effective G1 phase arrest. Besides, the number of cells stayed in sub-G1 phase also increased significantly after above treatments, in sequence with HPPPH@L@B > HPPPH@L > LND (Fig. 4b), confirming the effective cell cycle arrest induced by HPPPH@L@B again. The superior cell cycle arrest behavior of the HPPPH@L@B nanosystem could be explained that the delivery LND and BPTES in the nanosystem with high delivery efficiency could significantly inhibit glycolysis and glutamine metabolism, block the utilization of two important nutrients (glucose and glutamine) and dual-starve tumor cells, leading to the highest cell apoptosis ratio (Fig. 3a and b), DNA fragmentation and partial loss of genomic DNA fragments (Fig. 4a and b). These results collectively indicated that the HPPPH@L@B nanosystem could effectively induce tumor cells apoptosis and cell cycle arrest, leading to a significantly enhanced tumor killing.

3.4. Cellular metabolic suppression

Considering starvation treatment was closely related to the cellular

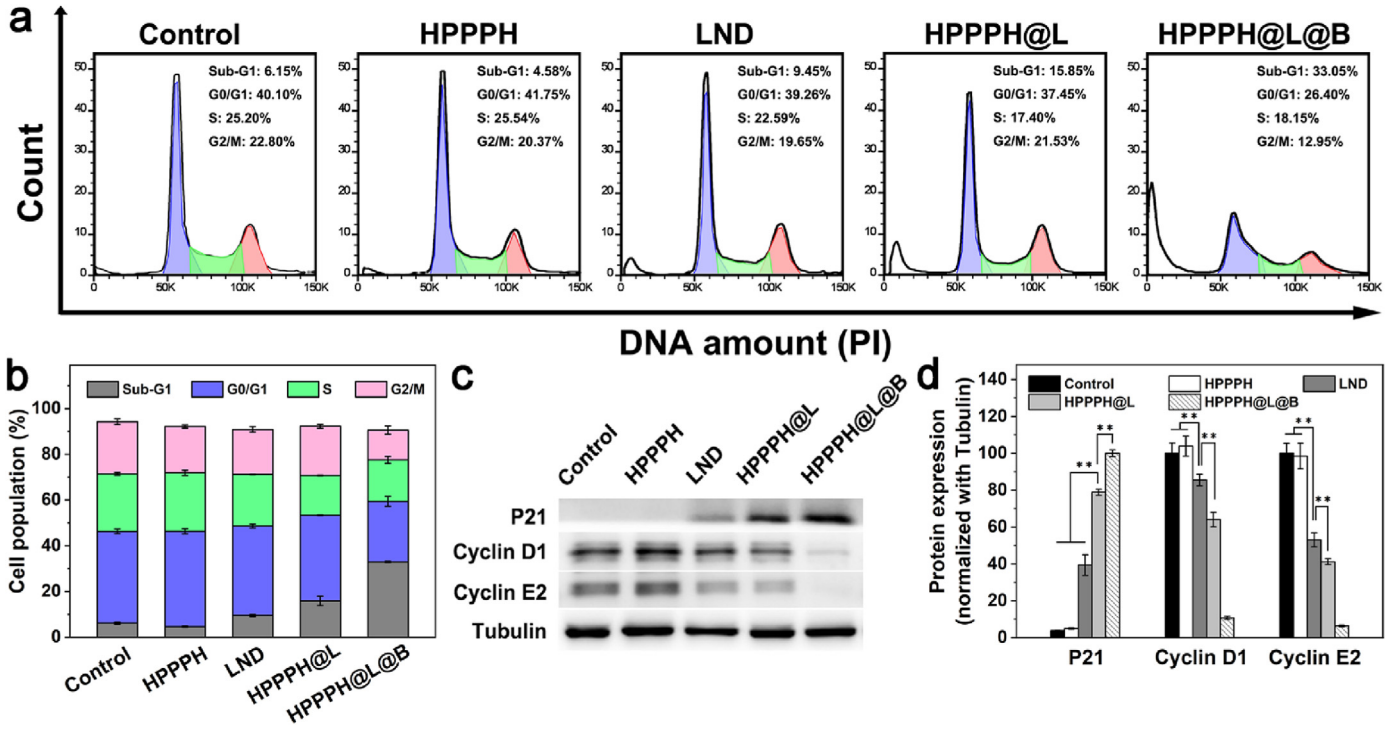

Fig. 4. Cell cycle arrest study. (a) Cell cycle analysis of MDA-MB-231 cells after treatment with PBS (control), HPPPH, LND, HPPPH@L and HPPPH@L@B for 24 h assessed by FCM with PI staining. (b) The corresponding percentage of cells in different phases of cell cycle were represented. (c) The expression level of cell cycle associated proteins in MDA-MB-231 cells was detected by Western blotting after above treatments for 24 h and (d) the corresponding quantitative analysis. Error bars present as mean ± SD (n = 6); **$p < 0.01$.

energy supply and metabolic changes, the ATP content and the changes of intracellular metabolites in tumor cells after administration were subsequently investigated using ATP detection kit and metabonomic technology, respectively. For intracellular ATP content determination, MDA-MB-231 cells were first co-incubated with HPPPH, LND, HPPPH@L and HPPPH@L@B for 24 h, the ATP content were then measured using ATP detection kit. As shown in Fig. 5a, there was no significant change in the content of intracellular ATP after treatment with HPPPH compared with control group, while the intracellular ATP content was slightly decreased in the LND group ($p < 0.05$). It could be explained that LND could actually reduces the level of glycolysis and causes the mitochondrial damage (Fig. 3c–e) [49-50], resulting in the inhibition of ATP production. It was worth noting that HPPPH@L induced more severe ATP depletion, demonstrating that HPPPH micelles can significantly improve LND utilization and anti-tumor effect. Most importantly, the HPPPH@L@B micelle nanosystem displayed the lowest intracellular ATP content among all treatments ($p < 0.01$), confirming again the excellent energy supply suppression and superior tumor starvation therapy effect. It might be benefited from the further inhibition of compensatory glutamine metabolism triggered by BPTES. Since BPTES could blocked the generation of the glutamic acid and oxoglutaric acid (also known as α-ketoglutaric acid) transformation through the glutamine metabolism inhibition, which were the raw material for supplying TCA cycle and the synthesis of various necessary biological compounds [7–10], the introduction of BPTES thus further inhibit the energy and material supply of tumor cells. It was the reason why HPPPH@L@B induced the highest degree of tumor cell apoptosis and cell cycle arrest.

In order to further verify the mechanism of the glucose and glutamine metabolism suppression caused by the HPPPH@L@B nanosystem, metabolomics was used to detect the changes of intracellular metabolites in tumor cells. As shown in Fig. 5b, the heat map displayed the overall change level of the differential metabolites in the tumor cells after incubation with different treatment groups. Briefly, there was no significant difference between the control and HPPPH negative groups, suggesting that the blank micelle nanocarrier had little effect on cell metabolism and exhibited the good biocompatibility. On the contrary, the levels of metabolites associated with glucose metabolism in MDA-MB-231 tumor cells displayed an obviously changed after co-incubation with LND for 24 h, which was attributed to the inherent inhibition of glucose metabolism induced by LND [4]. Furthermore, the amount of the differential metabolites of the LND-loaded micelle treatments (HPPPH@L and HPPPH@L@B groups) were significantly higher than that of LND group, in an order of LND < HPPPH@L < HPPPH@L@B, implying that the polymer micellar nanosystem combined with double-starvation therapy strategy could effectively altered the goal metabolism of tumor cells, leading to the desired tumor starvation effect. In detail, the statistical results of the typical substances related to glucose and glutamine metabolism were presented in Fig. 5c–f, including glucose 6-phosphate, lactic acid, glutamic acid and oxoglutaric acid. Typically, LND-loaded treatments (HPPPH@L and HPPPH@L@B) significantly induced the down-regulation of 6-phosphate-D-glucose and up-regulation of lactic acid in MDA-MB-231 cells compared with control, confirming the effective inhibition of glycolysis metabolism. LND could actually inhibit the hexokinase (a key limitation step among the glycolysis) and plasma membrane monocarboxylic acid transporter 4 (MCT4), which prevented the normal transport of lactate out of tumor cells [4]. Moreover, glutamate and oxoglutaric acid, as the two representative products of glutamine metabolism [12], were significantly down-regulated in the HPPPH@L@B treatment group compared with other groups, which was attributed to the introduction of glutamine metabolism inhibitors BPTES, implying the effective suppression of glutamine metabolism. This result indicated that the HPPPH@L@B nanosystem combined with dual-starvation therapy strategy could effectively inhibit glucose and glutamine metabolism, and accompanied with the severe energy depletion, substance supply deficiency, massive apoptosis and tumor cells cycle arrest, consequently contributing to the superior antitumor effect *in vitro*.

3.5. *In vivo* antitumor effect of HPPPH@L@B micelle nanosystem

To evaluate the antitumor efficacy of the HPPPH@L@B micelle nanosystem *in vivo*, MDA-MB-231 tumor cells-bearing BALB/c nude mice xenograft model was established. The tumor-bearing mice was then intravenously injected with different drug formulations twice per week and continued for 18 days (Fig. 6a). It was observed that all treatment groups exhibited various extents of tumor suppression compared to control (saline) and HPPPH negative control groups (Fig. 6b). Meanwhile, the HPPPH@L inhibited a relatively higher tumor inhibition degree than LND group, attributing to the superior drug delivery efficiency of the micellar nanosystem and the inherent antitumor effect of LND. Furthermore, the HPPPH@L@B micelle co-loaded with LND and BPTES showed the most outstanding tumor suppression among all treatments, which was in consistence with the analysis of relative tumor volume (Fig. 6c). Moreover, the HPPPH@L@B treatment also significantly prolonged the survival time of mice (Fig. 6d), implying the effective antitumor effect *in vivo*. The reasons could be explained as follows: (1) the HPPPH@L@B micelles with appropriate sizes were preferentially accumulated in tumor tissues and effectively internalized by tumor cells via EPR effect and HA receptor-mediated endocytosis; (2) the endocytosed nanosystem was then rapidly disassembled and *in situ* release LND and BPTES in response to the high concentration of GSH in cytoplasm, owing to the breakdown of the hydrophobicity-hydrophilicity balance maintained biostability of the micelle nanosystem; (3) the released LND and BPTES significantly inhibited the glycolysis and glutamine metabolism of the tumor cells, blocked the supply of energy and substance, leading to the desired tumor starvation and growth suppression. The results demonstrated that the HPPPH@L@B nanosystem could effectively inhibit the tumor growth *in vivo* through the dual-starvation therapy strategy.

The *in vivo* apoptosis and proliferation suppression were then investigated by the H&E staining, TUNEL (TdT-mediated dUTP Nick-End Labeling) and immunofluorescence detection of Ki67, respectively. As shown in Fig. 6e, LND, BPTES, HPPPH@L and HPPPH@L@B induced obviously apoptosis compared to control and HPPPH negative control groups, in an order of LND < BPTES < HPPPH@L < HPPPH@L@B, as revealed by the tissue structural fracture and chromatin condensation in the H&E images and the abundant magenta dots in the TUNEL staining analysis. Moreover, the lowest expression degree of Ki67 was found in the HPPPH@L@B group as well (Fig. 6e). Besides, the synergistic indexes of tumor volume (monitored by relative tumor volume), cell apoptosis (evaluated by TUNEL) and proliferation (assayed by the immunofluorescence staining of ki67) in the HPPPH@L@B were 5.05, 1.78 and 2.10 (Table S2), respectively. Above treatment confirmed again the synergistic effect with superior efficiency *in vivo* of HPPPH@L@B nanosystem.

To evaluate the biosafety of the HPPPH@L@B nanosystem, the changes of the body weight in the tumor-bearing mice after different administration were firstly monitored. It was observed that there was little change in body weight of mice in the HPPPH@L@B group (Fig. S11), suggesting the good biosafety. Secondly, the morphological and histological traits of the major tissues in the tumor-bearing mice after above treatments were examined using H&E staining assay. As expected, the normal and intact histological structure of the major tissues was displayed in the HPPPH@L@B group, as similar to the control group (Fig. 6f), indicating the excellent biocompatibility again. Last but not least, blood routine examination and biochemical analysis of the tumor-bearing mice were further performed after administration for 24 h. As shown in Fig. 6g, there also was no significant changes of the blood routine and biochemical indexes in the HPPPH@L@B group compared with control group (saline). These results confirmed that the HPPPH@L@B nanosystem possessed a good biosafety *in vivo*.

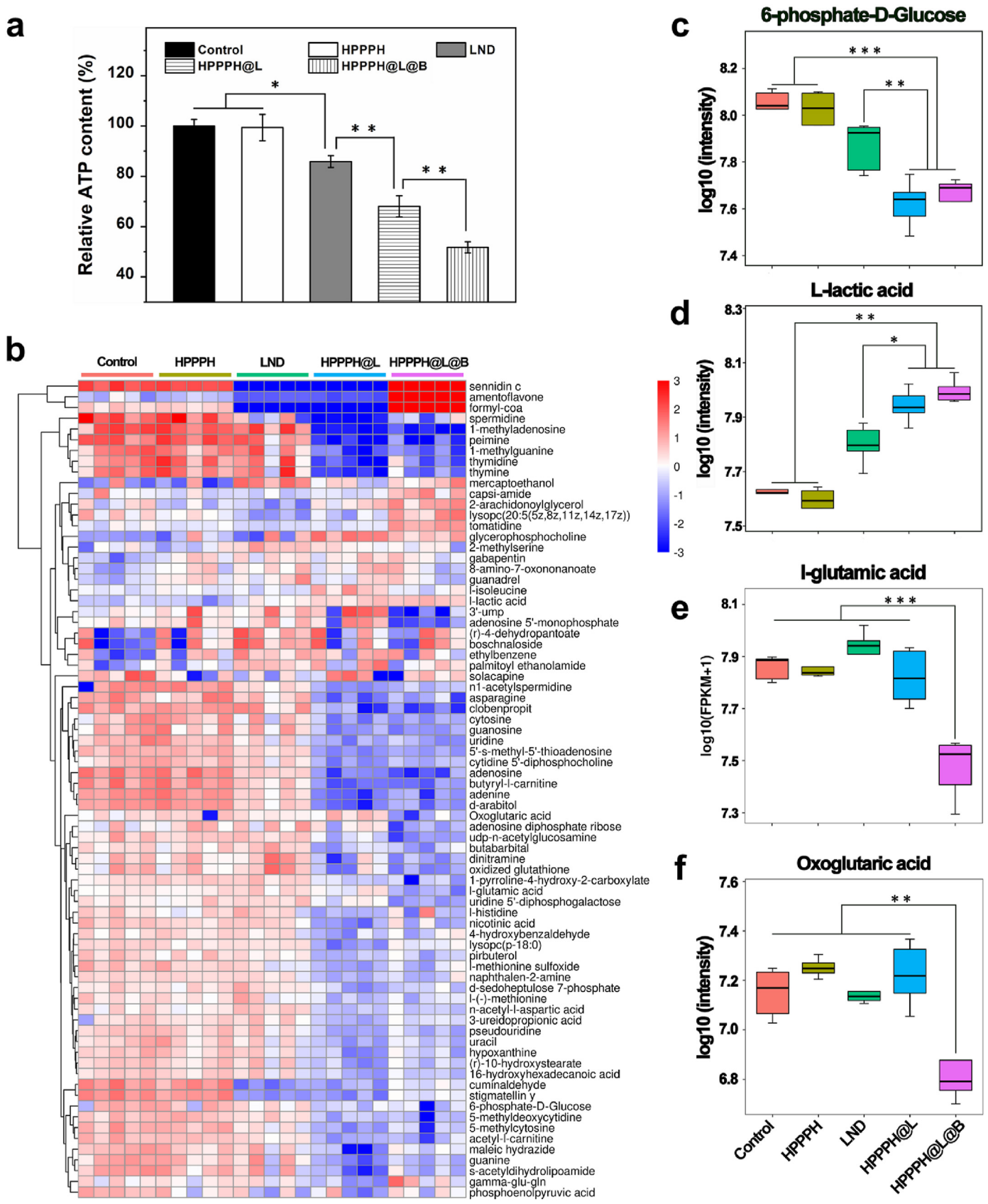

Fig. 5. Cell metabolic stress analysis. (a) Intracellular ATP content of MDA-MB-231 cells co-incubated with PBS, HPPPH, LND, HPPPH@L and HPPPH@L@B for 24 h, respectively. (b) Metabolomics study of MDA-MB-231 cells incubated with different formations for 24 h. Heat map showed the total levels of the differential metabolites and the statistical analysis of the presentative metabolites, including (c) 6-phosphate-D-glucose, (d) L-lactic acid, (e) L-glutamate and (f) oxoglutaric acid. Error bars present as mean ± SD (n = 6); *p < 0.05, **p < 0.01, ***p < 0.001.

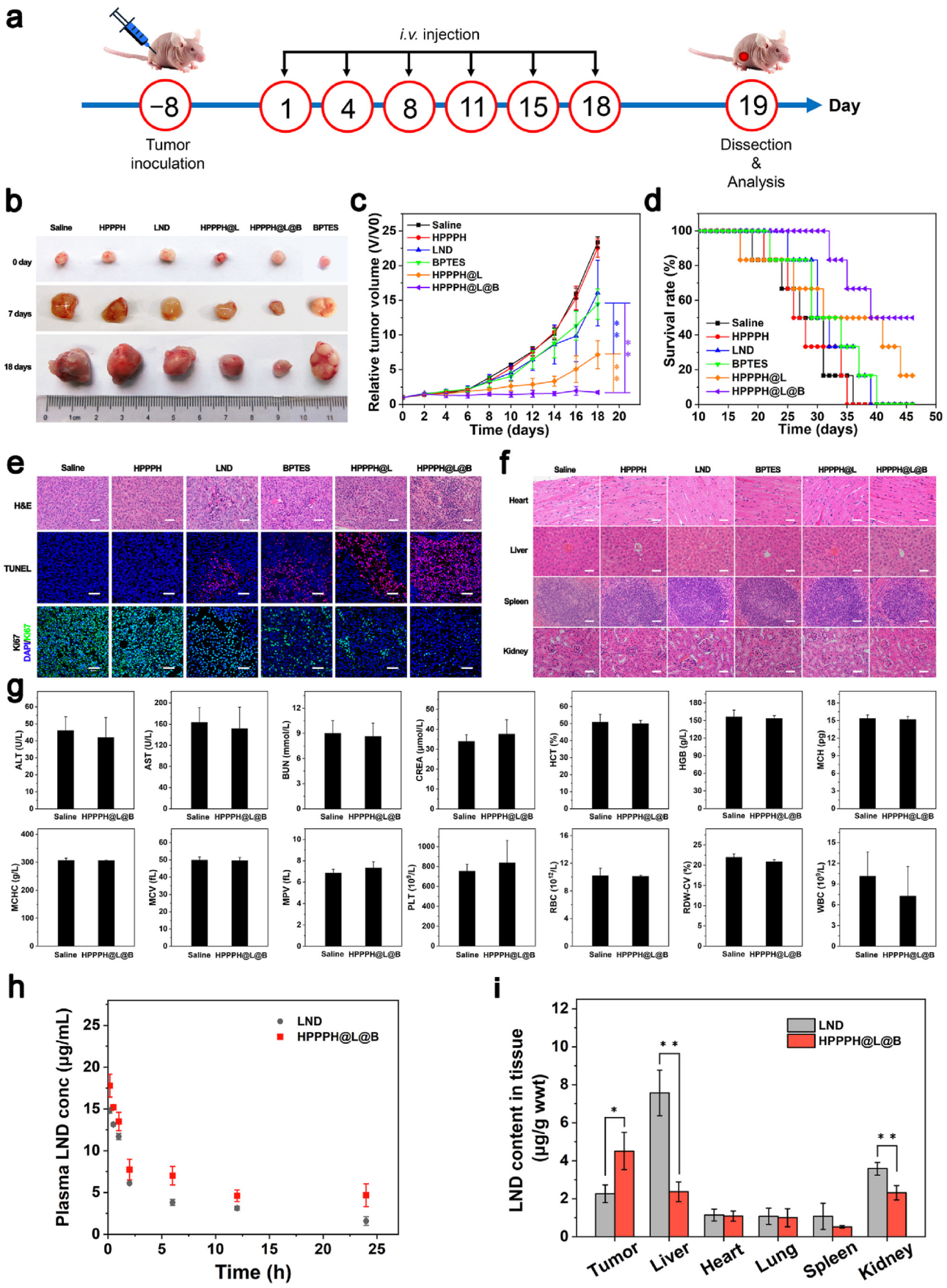

(caption on next page)

Fig. 6. Antitumor effect *in vivo*, biosafety evaluation, pharmacokinetics and biodistribution. (a) The BALB/c nude mice bearing MDA-MB-231 tumors were *i. v.* administrated with different formulations twice a week from day 0, which was defined as the 8th day post tumor inoculation. (b) Photographs of xenograft tumor of BALB/c nude mice after treatments with saline, HPPPH, LND, HPPPH@L, HPPPH@L@B for 0, 7, and 18 d, respectively. (c) The relative tumor volume and (d) survival rate of mice after above administrations. (e) H&E, TUNEL and Ki67 immunofluorescence staining images for tumors. (f) H&E staining images for heart, liver, spleen and kidney. (g) The blood biochemical levels and hematological indices of mice after 24 h of administration. (h) The pharmacokinetics of the LND and HPPPH@L@B micelles after intravenous injection into MDA-MB-231 cell tumor-bearing mice for various time intervals. (i) The biodistribution of the LND and HPPPH@L@B after 24 h post injection. Scale bars: 100 μm for (e) and (f). Error bars present as mean ± SD (n = 6); *p < 0.05, **p < 0.01.

To further evaluate the potential clinic application of the HPPPH@L@B nanosystem, the pharmacokinetics profile and biodistribution behavior of nanosystem in the tumor-bearing mice was investigated. Both the LND dosage in the blood and the main tissues were measured within treatment for 24 h. As for the pharmacokinetics assay, both LND and HPPPH@L@B micelle displayed the typical blood clearance curves, which was accordance with the two-compartment model. Furthermore, HPPPH@L@B micelle exhibited significantly longer circulation longevity than LND (Fig. 6h), indicating the prolonged circulation time. As for the biodistribution assay, the HPPPH@L@B nanosystem demonstrated significantly higher LND accumulation in the tumor tissues than LND (Fig. 6i, $p < 0.05$), while lower in liver and kidney ($p < 0.01$), suggesting the excellent tumor targeting with the reduced hepatorenal toxicity. All these data indicated that the HPPPH@L@B nanosystem combined dual-starvation therapy strategy displayed a superior antitumor effect with good biosafety *in vitro* and *in vivo*.

4. Conclusion

In summary, a redox-responsive micellar nanosystem co-loaded with glycolysis metabolism inhibitor LND and glutamine metabolism inhibitor BPTES was constructed for tumor targeted dual-starvation therapy. On the one hand, the fabricated nanosystem could specially uptake by tumor cells overexpressed HA receptor and rapidly release cargoes with high efficiency in response to the abundant GSH in the intratumoral cytoplasm. On other hand, the released LND and BPTES could simultaneously suppressed the glycolysis and glutamine metabolism and block the supply of the energy and substance, resulting in the significantly mitochondrial damage, cell cycle arrest, ATP deleting and tumor cells apoptosis with high efficiency. *In vitro* and *in vivo* results collectively demonstrated that the nanosystem combined with dual-starvation therapy exhibited a superior antitumor efficacy and reliable biosafety, which provided a high-performance and safe paradigm for malignant cancer treatment.

Credit author statement

Zhenxiang Fu: Data curation, Writing – original draft, Methodology. **Huiping Du:** Visualization, Writing – review & editing. **Siyu Meng:** Formal analysis, Investigation. **Mengjiao Yao:** Methodology, Validation. **Pan Zhao:** Investigation, Methodology. **Xiang Li:** Investigation, Validation. **Xinmin Zheng:** Investigation, Methodology. **Zhang Yuan:** Conceptualization. **Hui Yang:** Supervision. **Kaiyong Cai:** Project administration. **Liangliang Dai:** Funding acquisition, Writing – review & editing.

Declaration of competing interest

The authors declare that they have no known competing financial interests or personal relationships that could have appeared to influence the work reported in this paper.

Data availability

Data will be made available on request.

Acknowledgements

This work was financially supported by the National Natural Science Foundation of China (52003223), the Key R & D Program of Shaanxi Province (2022SF-012), the Fundamental Research Funds for the Central Universities (D5000220120) and the Young Talent Fund of University Association for Science and Technology in Shaanxi (20200302), China.

Appendix A. Supplementary data

Supplementary data to this article can be found online at https://doi.org/10.1016/j.mtbio.2022.100449.

References

[1] M.G. Vander Heiden, L.C. Cantley, C.B. Thompson, Understanding the Warburg effect: the metabolic requirements of cell proliferation, Science 324 (2009) 1029–1033, https://doi.org/10.1126/science.1160809.
[2] B. Faubert, A. Solmonson, R.J. DeBerardinis, Metabolic reprogramming and cancer progression, Science 368 (2020), https://doi.org/10.1126/science.aaw5473 eaaw5473.
[3] J.Q. Huang, L.P. Zhao, X. Zhou, L.S. Liu, R.R. Zheng, F.A. Deng, Y.B. Liu, X.Y. Yu, S.Y. Li, H. Cheng, Carrier free O_2-economizer for photodynamic therapy against hypoxic tumor by inhibiting cell respiration, Small 18 (2022), 2107467, https://doi.org/10.1002/smll.202107467.
[4] X.H. Liu, Y.H. Li, K.Y. Wang, Y.Y. Chen, M.W. Shi, X. Zhang, W. Pan, N. Li, B. Tang, GSH-responsive nanoprodrug to inhibit glycolysis and alleviate immunosuppression for cancer therapy, Nano Lett. 21 (2021) 7862–7869, https://doi.org/10.1021/acs.nanolett.1c03089.
[5] D. Cervantes-Madrid, Y. Romero, A. Dueñas-González, Reviving lonidamine and 6-diazo-5-oxo-l-norleucine to be used in combination for metabolic cancer therapy, BioMed Res. Int. 2015 (2015), 690492, https://doi.org/10.1155/2015/690492.
[6] A.A. Cluntun, M.J. Lukey, R.A. Cerione, J.W. Locasale, Glutamine metabolism in cancer: understanding the heterogeneity, Trends. Cancer. 3 (2017) 169–180, https://doi.org/10.1016/j.trecan.2017.01.005.
[7] M. Kodama, K. Oshikawa, H. Shimizu, S. Yoshioka, M. Takahashi, Y. Izumi, T. Bamba, C. Tateishi, T. Tomonaga, M. Matsumoto, K.I. Nakayama, A shift in glutamine nitrogen metabolism contributes to the malignant progression of cancer, Nat. Commun. 11 (2020) 1320, https://doi.org/10.1038/s41467-020-15136-9.
[8] M.H. Oh, I.H. Sun, L. Zhao, R.D. Leone, I.M. Sun, W. Xu, S.L. Collins, A.J. Tam, R.L. Blosser, C.H. Patel, J.M. Englert, M.L. Arwood, J.Y. Wen, Y. Chan-Li, L. Tenora, P. Majer, R. Rais, B.S. Slusher, M.R. Horton, J.D. Powell, Targeting glutamine metabolism enhances tumor-specific immunity by modulating suppressive myeloid cells, J. Clin. Invest. 130 (2020) 3865–3884, https://doi.org/10.1172/jci131859.
[9] N. Vidula, C. Yau, H.S. Rugo, Glutaminase (GLS) expression in primary breast cancer (BC): correlations with clinical and tumor characteristics, J. Clin. Oncol. 37 (2019) 558, https://doi.org/10.1200/jco.2019.37.15_suppl.558.
[10] A. Daemen, B. Liu, K. Song, M. Kwong, M. Gao, R. Hong, M. Nannini, D. Peterson, B.M. Liederer, C. Cruz, D. Sangaraju, A. Jaochico, X.F. Zhao, W. Sandoval, T. Hunsaker, R. Firestein, S. Latham, D. Sampath, M. Evangelista, G. Hatzivassiliou, Pan-cancer metabolic signature predicts co-dependency on glutaminase and de novo glutathione synthesis linked to a high-mesenchymal cell state, Cell Metabol. 28 (2018) 383–399, https://doi.org/10.1016/j.cmet.2018.06.003, e9.
[11] L.T. Jin, D. Li, G.N. Alesi, J. Fan, H.B. Kang, Z. Lu, T.J. Boggon, P. Jin, H. Yi, E.R. Wright, D. Duong, N.T. Seyfried, R. Egnatchik, R.J. DeBerardinis, K.R. Magliocca, C. He, M.L. Arellano, H.J. Khoury, D.M. Shin, F.R. Khuri, S. Kang, Glutamate dehydrogenase 1 signals through antioxidant glutathione peroxidase 1 to regulate redox homeostasis and tumor growth, Cancer Cell 27 (2015) 257–270, https://doi.org/10.1016/j.ccell.2014.12.006.
[12] A. Elgogary, Q.G. Xu, B. Poore, J. Alt, S.C. Zimmermann, L. Zhao, J. Fu, B.W. Chen, S.Y. Xia, Y.F. Liu, M. Neisser, C. Nguyen, R. Lee, J.K. Park, J. Reyes, T. Hartung, C. Rojas, R. Rais, T. Tsukamoto, G.L. Semenza, J. Hanes, B.S. Slusher, A. Le, Combination therapy with BPTES nanoparticles and metformin targets the metabolic heterogeneity of pancreatic cancer, Proc. Natl. Acad. Sci. USA 113 (2016) E5328–E5336, https://doi.org/10.1073/pnas.1611406113.
[13] Y.Q. Liu, X.J. Zhang, M.J. Zhou, X.Y. Nan, X.F. Chen, X.H. Zhang, Mitochondrial-targeting lonidamine-doxorubicin nanoparticles for synergistic chemotherapy to conquer drug resistance, ACS Appl. Mater. Interfaces 9 (2017) 43498–43507, https://doi.org/10.1021/acsami.7b14577.

[14] K. Shukla, D.V. Ferraris, A.G. Thomas, M. Stathis, B. Duvall, G. Delahanty, J. Alt, R. Rais, C. Rojas, P. Gao, Y. Xiang, C.V. Dang, B.S. Slusher, T. Tsukamoto, Design, synthesis, and pharmacological evaluation of bis-2-(5-phenylacetamido-1,2,4-thiadiazol-2-yl)ethyl sulfide 3 (BPTES) analogs as glutaminase inhibitors, J. Med. Chem. 55 (2012) 10551–10563, https://doi.org/10.1021/jm301191p.
[15] J.J. Xiang, Y.H. Shen, Y.F. Zhang, X. Liu, Q. Zhou, Z.X. Zhou, J.B. Tang, S.Q. Shao, Y.Q. Shen, Multipotent poly(tertiary amine-oxide) micelles for efficient cancer drug delivery, Adv. Sci. 9 (2022) 2200173, https://doi.org/10.1002/advs.202200173.
[16] Y. Lu, Z.G. Yue, J.B. Xie, W. Wang, H. Zhu, E. Zhang, Z.Q. Cao, Micelles with ultralow critical micelle concentration as carriers for drug delivery, Nat. Biomed. Eng. 2 (2018) 318–325, https://doi.org/10.1038/s41551-018-0234-x.
[17] M.W. Amjad, P. Kesharwani, M.C.I. Mohd Amin, A.K. Iyer, Recent advances in the design, development, and targeting mechanisms of polymeric micelles for delivery of siRNA in cancer therapy, Prog. Polym. Sci. 64 (2017) 154–181, https://doi.org/10.1016/j.progpolymsci.2016.09.008.
[18] Y. Kang, W. Sun, S.Y. Li, M.L. Li, J.L. Fan, J.J. Du, X.J. Liang, X.J. Peng, Oligo hyaluronan-coated silica/hydroxyapatite degradable nanoparticles for targeted cancer treatment, Adv. Sci. 6 (2019), 1900716, https://doi.org/10.1002/advs.201900716.
[19] Y.Q. Lv, X.M. Zhao, L.D. Zhu, S.J. Li, Q.Q. Xiao, W. He, L.F. Yin, Targeting intracellular MMPs efficiently inhibits tumor metastasis and angiogenesis, Theranostics 8 (2018) 2830–2845, https://doi.org/10.7150/thno.23209.
[20] G.D. Gong, J.Z. Pan, Y.X. He, J.J. Shang, X.L. Wang, Y.Y. Zhang, G.L. Zhang, F. Wang, G. Zhao, J.L. Guo, Self-assembly of nanomicelles with rationally designed multifunctional building blocks for synergistic chemo-photodynamic therapy, Theranostics 12 (2022) 2028–2040, https://doi.org/10.7150/thno.68563.
[21] Y.M. He, L. Lei, J. Cao, X.T. Yang, S.S. Cai, F. Tong, D. Huang, H. Mei, K. Luo, H.L. Gao, B. He, N.A. Peppas, A combinational chemo-immune therapy using an enzyme-sensitive nanoplatform for dual-drug delivery to specific sites by cascade targeting, Sci. Adv. 7 (2021) aba0776, https://doi.org/10.1126/sciadv.aba0776.
[22] F. Dosio, S. Arpicco, B. Stella, E. Fattal, Hyaluronic acid for anticancer drug and nucleic acid delivery, Adv. Drug Deliv. Rev. 97 (2016) 204–236, https://doi.org/10.1016/j.addr.2015.11.011.
[23] B.Y. Niu, K.X. Liao, Y.X. Zhou, T. Wen, G.L. Quan, X. Pan, C.B. Wu, Application of glutathione depletion in cancer therapy: enhanced ROS-based therapy, ferroptosis, and chemotherapy, Biomaterials 277 (2021), 121110, https://doi.org/10.1016/j.biomaterials.2021.121110.
[24] H.X. Tang, C.Q. Li, Y. Zhang, H.Y. Zheng, Y. Cheng, J.J. Zhu, X.J. Chen, Z.H. Zhu, J.G. Piao, F.Z. Li, Targeted Manganese doped silica nano GSH-cleaner for treatment of liver cancer by destroying the intracellular redox homeostasis, Theranostics 10 (2020) 9865–9887, https://doi.org/10.7150/thno.46771.
[25] K.C. Liang, H.T. Sun, Z.B. Yang, H.Z. Yu, J. Shen, X.L. Wang, H.R. Chen, Breaking the redox homeostasis: an albumin-based multifunctional nanoagent for GSH depletion-assisted chemo-/chemodynamic combination therapy, Adv. Funct. Mater. 31 (2021), 2100355, https://doi.org/10.1002/adfm.202100355.
[26] L.L. Dai, X. Li, X.L. Duan, M.H. Li, P.Y. Niu, H.Y. Xu, K.Y. Cai, H. Yang, A pH/ROS cascade-responsive charge-reversal nanosystem with self-amplified drug release for synergistic oxidation-chemotherapy, Adv. Sci. 6 (2019), 1801807, https://doi.org/10.1002/advs.201801807.
[27] J.R. Gardner, R.H. Zhang, R. Rose, S. McKenzie, P. Maslak, M.L. Heaney, Malignant cells in the marrow and blood of patients with hematopoietic malignancies have higher mitochondrial membrane potential as measured with the potentiometric dye JC-1, Blood 108 (2006) 2367, https://doi.org/10.1182/blood.v108.11.2367.2367.
[28] L.L. Dai, Y.L. Yu, Z. Luo, M.H. Li, W.Z. Chen, X.K. Shen, F. Chen, Q. Sun, Q.F. Zhang, H. Gu, K.Y. Cai, Photosensitizer enhanced disassembly of amphiphilic micelle for ROS-response targeted tumor therapy in vivo, Biomaterials 104 (2016) 1–17, https://doi.org/10.1016/j.biomaterials.2016.07.002.
[29] Z.X. Meng, X.S. Zhang, H.Y. Tan, H. Lian, Zinc-enriched nanosystem for dual glycolysis regulation and photothermal therapy to synergistically inhibit primary melanoma and lung metastasis, Chem. Eng. J. 435 (2022), 134781, https://doi.org/10.1016/j.cej.2022.134781.
[30] L.Z. Li, C.Y. Jiang, L.J. Navsaria, Y. Liu, A. Leeming, M. Wang, Y.X. Yao, Targeting glutamine metabolism overcomes resistance to targeted therapies in refractory mantle cell lymphoma, Blood 136 (2020) 25–26, https://doi.org/10.1182/blood-2020-140736.
[31] X.H. Wang, M. Li, K.B. Ren, C.Y. Xia, J.P. Li, Q.W. Yu, Y. Qiu, Z.Z. Lu, Y. Long, Z.R. Zhang, Q. He, On-demand autophagy cascade amplification nanoparticles precisely enhanced oxaliplatin-induced cancer immunotherapy, Adv. Mater. 32 (2020), 2002160, https://doi.org/10.1002/adma.202002160.
[32] M. Wen, N. Yu, S.W. Wu, M.M. Huang, P. Qiu, Q. Ren, M.F. Zhu, Z.G. Chen, On-demand assembly of polymeric nanoparticles for longer-blood-circulation and disassembly in tumor for boosting sonodynamic therapy, Bioact. Mater. 18 (2022) 242–253, https://doi.org/10.1016/j.bioactmat.2022.03.009.
[33] X. Wang, M.H. Li, Y.H. Hou, Y.A. Li, X.M. Yao, C.C. Xue, Y. Fei, Y. Xiang, K.Y. Cai, Y.L. Zhao, Z. Luo, Tumor-microenvironment-activated in situ self-assembly of sequentially responsive biopolymer for targeted photodynamic therapy, Adv. Funct. Mater. 30 (2020), 2000229, https://doi.org/10.1002/adfm.202000229.
[34] G. Chang, J. Wang, H. Zhang, Y. Zhang, C. Wang, H. Xu, H. Zhang, Y. Lin, L. Ma, Q. Li, T. Pang, CD44 targets Na^+/H^+ exchanger 1 to mediate MDA-MB-231 cells' metastasis via the regulation of ERK1/2, Brit, J. Cancer 110 (2014) 916–927, https://doi.org/10.1038/bjc.2013.809.
[35] L.L. Dai, Q.F. Zhang, X.K. Shen, Q. Sun, C.Y. Mu, H. Gu, K.Y. Cai, A pH-responsive nanocontainer based on hydrazone-bearing hollow silica nanoparticles for targeted tumor therapy, J. Mater. Chem. B. 4 (2016) 4594–4604, https://doi.org/10.1039/c6tb01050d.
[36] Y.Y. Kong, G.G. Chen, Z.J. Xu, G. Yang, B. Li, X.S. Wu, W.Q. Xiao, B.Q. Xie, L.N. Hu, X. Sun, G.M. Chang, M.J. Gao, L. Gao, B.J. Dai, Y. Tao, W.L. Zhu, J.M. Shi, Pterostilbene induces apoptosis and cell cycle arrest in diffuse large B-cell lymphoma cells, Sci. Rep. 6 (2016), 37417, https://doi.org/10.1038/srep37417.
[37] H.B. Ruttala, N. Chitrapriya, K. Kaliraj, T. Ramasamy, W.H. Shin, J.H. Jeong, J.R. Kim, S.K. Ku, H.G. Choi, C.S. Yong, J.O. Kim, Facile construction of bioreducible crosslinked polypeptide micelles for enhanced cancer combination therapy, Acta Biomater. 63 (2017) 135–149, https://doi.org/10.1016/j.actbio.2017.09.002.
[38] P.J. Burke, Mitochondria, bioenergetics and apoptosis in cancer, Trends. Cancer. 3 (2017) 857–870, https://doi.org/10.1016/j.trecan.2017.10.006.
[39] M.G. Vander Heiden, N.S. Chandel, E.K. Williamson, P.T. Schumacker, C.B. Thompson, Bcl-x_L regulates the membrane potential and volume homeostasis of mitochondria, Cell 91 (1997) 627–637, https://doi.org/10.1016/s0092-8674(00)80450-x.
[40] X.B. Cao, J.L. Yap, M.K. Newell-Rogers, C. Peddaboina, W.H. Jiang, H.T. Papaconstantinou, D. Jupitor, A. Rai, K.Y. Jung, R.P. Tubin, W. Yu, K. Vanommeslaeghe, P.T. Wilder, A.D. MacKerell, S. Fletcher, R. W Smythe, The novel BH3 α-helix mimetic JY-1-106 induces apoptosis in a subset of cancer cells (lung cancer, colon cancer and mesothelioma) by disrupting Bcl-xL and Mcl-1 protein–protein interactions with Bak, Mol. Cancer 12 (2013) 42, https://doi.org/10.1186/1476-4598-12-42.
[41] C. Wu, C.L. Wang, Y.Y. Zheng, Y.X. Zheng, Z.Q. Liu, K.M. Xu, W.Y. Zhong, Triple enzyme-regulated molecular hydrogels for carrier-free delivery of lonidamine, Adv. Funct. Mater. 31 (2021), 2104418, https://doi.org/10.1002/adfm.202104418.
[42] Y. Liu, J. Zhang, Y. Tu, L. Zhu, Potential-independent intracellular drug delivery and mitochondrial targeting, ACS Nano 16 (2022) 1409–1420, https://doi.org/10.1021/acsnano.1c09456.
[43] L. Wang, H. Zhou, Y. Wang, G. Cui, L.J. Di, CtBP maintains cancer cell growth and metabolic homeostasis via regulating SIRT4, Cell Death Dis. 6 (2015), e1620, https://doi.org/10.1038/cddis.2014.587.
[44] W.J. Xu, I.A. Siddiqui, M. Nihal, S. Pilla, K. Rosenthal, H. Mukhtar, S.Q. Gong, Aptamer-conjugated and doxorubicin-loaded unimolecular micelles for targeted therapy of prostate cancer, Biomaterials 34 (2013) 5244–5253, https://doi.org/10.1016/j.biomaterials.2013.03.006.
[45] H. Cai, X.H. Dai, X.M. Wang, P. Tan, L. Gu, Q. Luo, X.L. Zheng, Z.Q. Li, H.Y. Zhu, H. Zhang, Z.W. Gu, Q.Y. Gong, K. Luo, A nanostrategy for efficient imaging-guided antitumor therapy through a stimuli-responsive branched polymeric prodrug, Adv. Sci. 7 (2020), 1903243, https://doi.org/10.1002/advs.201903243.
[46] D. Findakly, K. Beedupalli, Mammary analog secretory carcinoma in adults: a systematic review, J. Clin. Oncol. 40 (2022), https://doi.org/10.1200/JCO.2022.40.16_suppl.e18076 e18076-e18076.
[47] Q.Y. Hao, Z.M. Huang, Q. Li, D.X. Liu, P.W. Wang, K. Wang, J.Q. Li, W. Cao, W.H. Deng, K. Wu, R. Su, Z.M. Liu, J. Vadgama, Y. Wu, A novel metabolic reprogramming strategy for the treatment of diabetes-associated breast cancer, Adv. Sci. 9 (2022), 2102303, https://doi.org/10.1002/advs.202102303.
[48] A. Lewinska, J. Adamczyk-Grochala, A. Deregowska, M. Wnuk, Sulforaphane-induced cell cycle arrest and senescence are accompanied by DNA hypomethylation and changes in microRNA profile in breast cancer cells, Theranostics 7 (2017) 3461–3477, https://doi.org/10.7150/thno.20657.
[49] L.L. Guo, A.A. Shestov, A.J. Worth, K. Nath, D.S. Nelson, D.B. Leeper, J.D. Glickson, I.A. Blair, Inhibition of mitochondrial complex II by the anticancer agent lonidamine, J. Biol. Chem. 291 (2016) 42–57, https://doi.org/10.1074/jbc.m115.697516.
[50] J.J. Gu, A. Singh, C. Mavis, V. Yanamadala, K. Xue, M. Grau, P. Lenz, G. Lenz, M.S. Czuczman, F. Hernandez, Up-regulation of hexokinase II (HK) alters the glucose metabolism and disrupts the mitochondrial potential in aggressive B-cell lymphoma contributing to Rituximab-chemotherapy resistance and is a clinically relevant target for future therapeutic development, Blood 124 (2014) 1767, https://doi.org/10.1182/blood.V124.21.1767.1767.